

Compliance Boundary Conditions for Patient-Specific Deformation Simulation Using the Finite Element Method

Ece Ozkan and Orcun Goksel

Computer-assisted Applications in Medicine Group, ETH Zurich, Switzerland

E-mail: {eozkan,ogoksel}@vision.ee.ethz.ch

Abstract

Tissue deformation simulations for pre-operative planning or intra-operative guidance of medical procedures require accurate patient-specific models and are commonly performed using the Finite Element Method (FEM). Since only a small part of the entire body is typically observed with medical imaging, the deformation models are often limited to a relatively small region-of-interest (ROI). Surrounding this ROI, one then needs to define suitable boundary conditions for an accurate simulation. Conventionally, boundary conditions are set arbitrarily or heuristically at chosen model locations; typically as either zero-displacement or -force constraint, which obviously are suboptimal where ROI borders are neither fixed (e.g. on bone) or free (e.g. skin facing the air). In this work, we present a novel boundary-condition formulation, called *compliance boundary conditions* (CBC), which approximate the effect of anatomy outside this ROI and augment this onto the ROI border nodes. CBC can be parametrized from observed tissue displacements, e.g. tracked in ultrasound (US) or magnetic-resonance imaging (MRI). It is inherently embedded in the FEM deformation model to be used for computing any interaction response. CBC is a generalization of conventional boundary constraints, where the typical zero-displacement and -force constraints are obtained at the two extremes of the given CBC parameter. We demonstrate CBC for linear- and quadratic-strain FEM models in 2D and 3D numerical phantoms, for which different element/integration formulations and the effect of noise are studied. CBC is shown to reduce displacement errors for both 2D and 3D numerical phantoms by more than 50% compared to conventional boundary conditions. We also present CBC on tissue-mimicking gelatin phantom experiments from displacements observed in US images. In an application scenario of simulating needle insertion for prostate brachytherapy, CBC is shown to reduce seed placement errors by more than 70% compared to conventional boundary conditions.

1. Introduction

Patient-specific tissue deformation simulation is essential for pre-operative planning and intra-operative guidance of medical interventions and, accordingly, has been a major research interest in the last decades. Deformable tissue models enable the simulation of anatomical motion and displacements, which in turn allows for anticipating deviations in

interventional target locations such as in brachytherapy and biopsy of the breast, liver, and the prostate. These models include the physical properties and the geometry of an anatomical region-of-interest (ROI). They enable the computation of tissue deformation, e.g., due to respiration (Clifford et al. 2002; Eom et al. 2010; Preiswerk et al. 2014) and medical tool interactions (Dehghan et al. 2008; Misra et al. 2008; Goksel et al. 2011).

In contrast to other deformation models, such as mass-spring mesh models (Harders et al. 2003; Mollemans et al. 2004) and finite differences (Debunne et al. 2001), the Finite Element Method (FEM) is a well-established technique based on continuum-mechanics. In FEM, the continuum is discretized spatially into simpler geometric elements the mechanical responses of which can easily be computed as integrals (Becker and Teschner 2007; Peterlik et al. 2012). With such discretization (mesh) and its elastic composition (i.e., Young’s modulus and Poisson’s ratio) as well as boundary conditions on a model, the deformation outcome can then be found by solving partial differential equations. For precisely assigning elastic maps to meshes, the anatomical region is often first segmented from medical images, such as CT, MRI, or US, e.g. Sharma and Aggarwal 2010; Goksel and Salcudean 2011.

Patient-specific models are often limited to a relatively small region-of-interest (ROI), since only a smaller part of the entire anatomy can (or is chosen to) be imaged for practical reasons, e.g., to minimize irradiation in CT, to minimize scan-time in MRI, or due to the smaller field-of-view of US. Then, a major question becomes how to set the boundary constraints around such ROI. Note that the boundary constraints on some regions are easy to define: For instance, it is reasonable to use zero-displacement (fixed) constraints for the tissue “fixed” to (neighbouring) rigid structures, e.g. bones; and to use zero-force (free) constraints for the skin (neighbouring the air). Accordingly, the ideal case is when the anatomy to be simulated is separated from the rest of the body through natural anatomical constraints, i.e. bones and the skin, within the ROI. For example, an image of the entire breast including the ribs and the skin would allow for an effective *confined* model with boundary constraints that can be precisely defined. Nevertheless, for most other anatomy, such natural boundaries do not exist or not lie within typical imaging ROI. For instance, the visceral structures are all in contact with each other; therefore, even if a small section of viscera is imaged or chosen to be simulated for numerical reasons, its interaction with the rest of the abdomen and thorax should be taken into account for an accurate simulation. Many deformation simulations, however, ignore such interaction outside the ROI by simply using zero-displacement or -force boundary constraints on the outer surfaces (Ayache et al. 1998; Hensel et al. 2007; Goksel et al. 2011; Lee et al. 2012; Li et al. 2013).

Some studies pad the ROI with superfluous tissue, in order to vanish simulation artifacts inside the intended ROI caused by constraints assumed at the outer boundaries (Lasso et al. 2010; Cui et al. 2014). Not only this adds to computational cost, but it is also not well-defined how far and with which tissue to pad; besides, no guarantees can be given on whether and how closely actual ROI deformations can be approximated with such added margin. An alternative is to use natural anatomical constraints

mentioned above; e.g. the rib-cage as fixed during breast interventions (Didier et al. 2007). Nevertheless, this can only account for such structures given that they are entirely within the ROI, and this also requires segmenting these structures, which is an additional (often burdensome and error-prone) preprocessing step.

There are only few studies on boundary conditions. In Plantefevé et al. 2014, a statistical atlas is obtained from multiple patients for the organ of interest and the boundary conditions are defined according to the mean position and variance available in the atlas. This was introduced for estimating bilateral boundary conditions, but how to define the boundary constraints for contacts with surrounding organs is an outstanding question. Despite the potential of population approaches, patient-specific models are known to be superior and preferred, where possible. In Roose et al. 2008, the authors propose to iteratively update boundary constraints within a surface and image-intensity registration framework, but this framework requires segmentations or landmark points for matching. In Ahmadian et al. 2001, boundary conditions on beam structures are extracted for a civil engineering application using a boundary stiffness matrix from characteristic equations by formulating them as non-linear equations from the measured natural frequencies of the structure.

Elasticity parameterization of FEM models has been extensively studied using both image registration and biomechanical elastography techniques. In contrast, to the best of our knowledge, modeling boundary conditions for biomechanical simulations has received little to no attention in the literature, despite boundary conditions being arguably more important for deformation response than the elasticity parameters, discretization, and the choice of the model (Koch et al. 1996; Misra et al. 2009). In order to demonstrate this with a motivating example, we compared the displacements of different setups with an inclusion phantom seen in Fig.1(a). The model was assumed to have zero-displacement constraint (fixed) at the bottom surface. In Fig.1(b), two different elasticity parameters are used with half and double the Young's modulus for the inclusion. In Fig.1(c), a coarser mesh is used to model the discretization errors. In Fig.1(d), geometrical and material non-linearity are simulated separately for comparison with the linear case. In Fig.1(e), different boundary conditions are compared using additional sliding displacement constraints on the side surfaces, as well as only the corners being constrained. Change of mean displacements normalized with the maximum displacement, Δ , is computed for different setups as shown in the figure titles. It is observed in this example that different boundary condition settings have significantly more impact on the deformation response than any other model parameter.

Artificial boundary conditions have been studied as absorbing boundaries for acoustic propagation and to limit numerical computations in areas such as seismology, weather prediction and fluid dynamics, e.g. Engquist and Majda 1977; Engquist and Majda 1979; Nataf 2013; Sauter and Schanz 2017. Nevertheless, to the best of our knowledge, modeling boundaries has received little attention for deformable solid simulation, such as in medical applications.

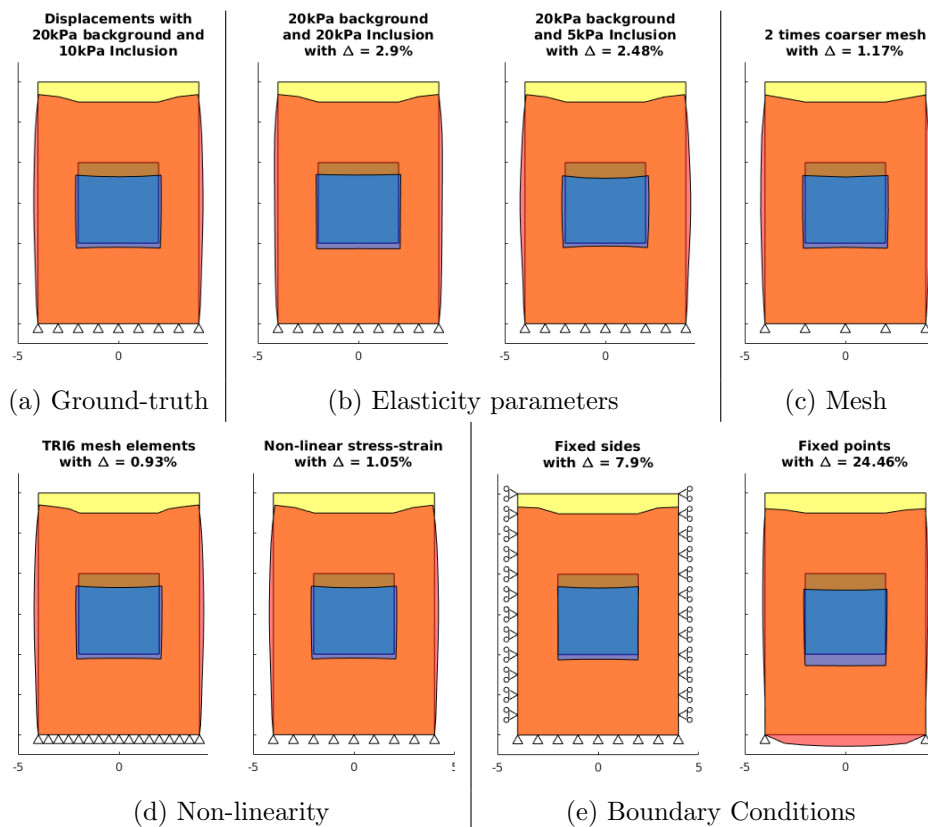


Figure 1. (a) A baseline simulation of 80×120 mm numerical phantom of 20 kPa Young’s modulus, 0.49 Poisson’s ratio, 10 mm depth, and displacement-constrained at bottom surface; having a 10 kPa 40×40 mm inclusion, modeled using plane-stress assumption and linear Hookean response with a triangular (TRI3) discretization with 213 nodes. We compare different model parameters and choices: (b) inclusion elasticity parameters of 20 kPa and 5 kPa; (c) a coarser mesh of 145-node TRI3 elements; (d) quadratic TRI6 elements for geometric non-linearity and nonlinear stress-strain model for material nonlinearity; and (e) different boundary conditions with sliding side surfaces or only the two corners fixed. Boundary condition choice is seen to make the largest difference in deformation response.

In this work, we study *compliance boundary conditions* (CBC), which can be naturally represented and solved in the standard FEM framework by embedding their representation into the well-known stiffness matrix formulation. Preliminary results of this work was presented at a conference (Ozkan and Goksel 2015) with basic simulation experiments for elastic materials. Herein, we present CBC for various 2D and 3D FEM element formulations as well as for a nonlinear (hyperelastic) material formulation. We also show results from a tissue-mimicking phantom with deformation data acquired by ultrasound imaging.

2. Methods

Conventionally, deformation boundary conditions are set arbitrarily or hand-crafted for a given simulation scenario. The work-flow of proposed CBC is shown in Fig. 2, where

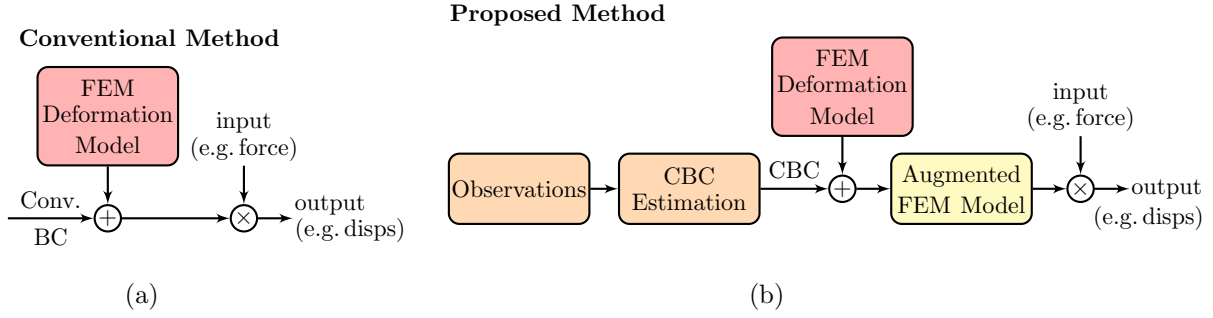


Figure 2. FEM with (a) conventional boundary conditions and (b) our compliance boundary conditions (CBC).

the deformation effects of boundaries are modeled from observations, with which the deformation model is augmented to incorporate their effect.

2.1. Simulating Tissue Deformation

Let an anatomical region be discretized by N mesh nodes into finite elements. This model is then characterized by FEM through the following linear system

$$\mathbf{K}\mathbf{u} = \mathbf{f}, \tag{1}$$

where $\mathbf{K} \in \mathbb{R}^{DN \times DN}$ is the sparse positive-definite symmetric stiffness matrix dependent on the geometry and biomechanical properties of the elements, $\mathbf{u} \in \mathbb{R}^{DN}$ is the vector of nodal displacements and $\mathbf{f} \in \mathbb{R}^{DN}$ is the vector of nodal forces with D being the spatial dimension. Boundary constraints are then imposed on such model, and subsequently the deformation can be estimated by solving the system of equations.

To generate \mathbf{K} , local elasticity distribution in tissue has to be known. These maps for deformation simulation are often generated by segmenting the anatomy to assign generic elasticity properties within each major structure (Hensel et al. 2007; Lasso et al. 2010; Goksel et al. 2011; Cui et al. 2014). Alternatively, elastography is an emerging technique to reconstruct local elasticity parameters that make up \mathbf{K} (Kallel and Ophir 1997; Doyley et al. 2000; Manduca et al. 2001; Eskandari et al. 2008). As this is not the focus of this paper, we assume below that an approximate elasticity distribution in the ROI is given, i.e. \mathbf{K} is known. Accordingly, we focus instead on estimating boundary conditions from deformation observations for a given elasticity distribution.

2.2. Relation Between Full and Limited ROI Model

To illustrate the problem, consider that an accurate FEM model of the *entire* body (not only of the ROI) exists and is available to us. As mentioned above, this is often unlikely due to limited imaging field-of-view, imaging time constraints, radiation exposure, etc. Nevertheless, this assumption will facilitate below the formulation of the

relation between the ROI boundary conditions and the full anatomical model, and in turn the derivation of CBC parametrization as an approximation of such relation.

Without loss of generality, the nodes of full FEM model \mathbf{K}_f can be reordered with the *observed* nodes (inside ROI) first, followed by the *unobserved* nodes (outside ROI). The full-model linear system can then be rewritten as

$$\mathbf{K}_f \mathbf{u}_f = \begin{bmatrix} \mathbf{K}_{oo} & \mathbf{K}_{ou} \\ \mathbf{K}_{ou}^T & \mathbf{K}_{uu} \end{bmatrix} \begin{bmatrix} \mathbf{u}_o \\ \mathbf{u}_u \end{bmatrix} = \begin{bmatrix} \mathbf{f}_o \\ \mathbf{f}_u \end{bmatrix} = \mathbf{f}_f, \quad (2)$$

$$\Rightarrow \begin{cases} \mathbf{K}_{oo} \mathbf{u}_o + \mathbf{K}_{ou} \mathbf{u}_u = \mathbf{f}_o & (3) \\ \mathbf{K}_{ou}^T \mathbf{u}_o + \mathbf{K}_{uu} \mathbf{u}_u = \mathbf{f}_u & (4) \end{cases}$$

where \mathbf{u}_o and \mathbf{u}_u contain the displacements at, respectively, the observed ROI and unobserved outer nodes. From (4), it follows that $\mathbf{u}_u = \mathbf{K}_{uu}^{-1}(\mathbf{f}_u - \mathbf{K}_{ou}^T \mathbf{u}_o)$. Using this equation in (3) and algebraic manipulations yield the force-displacement relationship for observed ROI nodes as

$$\underbrace{\mathbf{f}_o - \mathbf{K}_{ou} \mathbf{K}_{uu}^{-1} \mathbf{f}_u}_{\tilde{\mathbf{f}}_o} = \underbrace{(\mathbf{K}_{oo} - \mathbf{K}_{ou} \mathbf{K}_{uu}^{-1} \mathbf{K}_{ou}^T)}_{\tilde{\mathbf{K}}_{oo}} \mathbf{u}_o, \quad (5)$$

where $\tilde{\mathbf{K}}_{oo}$ is the so-called *condensed* stiffness matrix (Bro-Nielsen and Cotin 1996). A sample condensed stiffness matrix for the ROI mesh in Fig. 3(a) is depicted in Fig. 3(b). This condensed system in (5) can then model ROI deformation *exactly* as if the full anatomical model were present.

Since the geometry and elasticity parameters of the full model are not always observable as mentioned earlier, the condensed stiffness matrix $\tilde{\mathbf{K}}_{oo}$ cannot be deduced directly in practice. Nevertheless, if the incremental difference \mathbf{C} between such condensed system and an (isolated) ROI model \mathbf{K} can be approximated, then the condensed system could be reconstructed as

$$\tilde{\mathbf{K}}_{oo} = \mathbf{K} + \mathbf{C}. \quad (6)$$

Our approach is to approximate \mathbf{C} from deformation observations. This will then enable the known \mathbf{K} to be augmented into an *approximate* condensed system, using which any interaction response can be computed similarly to the expected deformation response of the (unknown) full model \mathbf{K}_f . Such \mathbf{C} would in essence “encode” the effect of the full model onto the boundary nodes of the smaller ROI model. For example, for the 2D example in Fig. 3(a), such difference \mathbf{C} should look like Fig. 3(c), where the non-zero elements are at rows/columns corresponding to ROI boundary nodes. These elements than represent neither zero-displacement nor zero-force constraints, but rather act like *compliant* (spring-like) due to the lumped effect of surrounding soft tissue; thus, we call this augmentation *compliance boundary conditions* (CBC).

2.3. Estimating Compliance Boundary Conditions

Assuming no external force is applied on unobserved nodes, i.e. $\mathbf{f}_u = 0$, then (5) becomes $\mathbf{f}_o = \tilde{\mathbf{K}}_{oo} \mathbf{u}_o = (\mathbf{K} + \mathbf{C}) \mathbf{u}_o$. Consider that the nodes of the augmented ROI stiffness

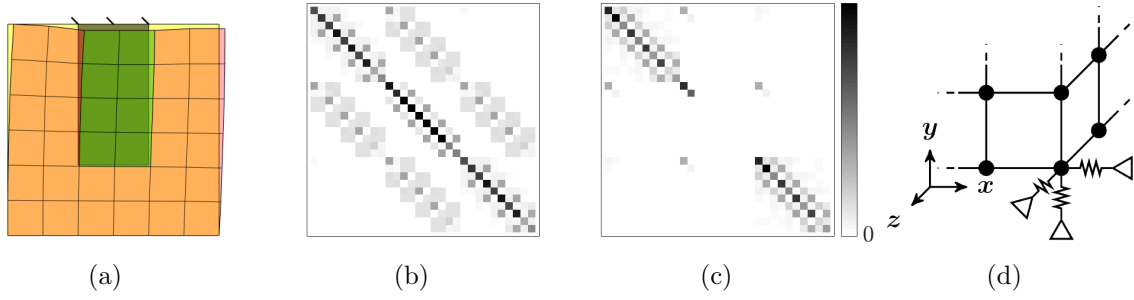


Figure 3. (a) An (*unobserved*) full model in orange and the (*observed*) ROI in green, where the entire bottom surface is fixed and the top surface of ROI is compressed diagonally. Element-wise magnitude of (b) a condensed stiffness matrix $\tilde{\mathbf{K}}_{oo}$ and (c) an incremental difference matrix \mathbf{C} are shown. (d) CBC for *diag* approximation is illustrated to correspond to an axis-aligned spring model.

matrix $\tilde{\mathbf{K}}_{oo}$ are ordered with the boundary ROI nodes first, followed by the internal ROI nodes. The linear system can then be rewritten as a block matrix system as follows

$$\tilde{\mathbf{K}}_{oo}\mathbf{u}_o = \begin{bmatrix} \mathbf{K}_{bb} + \mathbf{C}_{bb} & \mathbf{K}_{bi} + \mathbf{C}_{bi} \\ \mathbf{K}_{bi}^T + \mathbf{C}_{bi}^T & \mathbf{K}_{ii} + \mathbf{C}_{ii} \end{bmatrix} \begin{bmatrix} \mathbf{u}_b \\ \mathbf{u}_i \end{bmatrix} = \begin{bmatrix} \mathbf{f}_b \\ \mathbf{f}_i \end{bmatrix} = \mathbf{f}_o, \quad (7)$$

where \mathbf{u}_b and \mathbf{u}_i contain the displacements at the boundary and internal ROI nodes, respectively. Since \mathbf{C} has non-zero elements only at rows and columns corresponding to the boundary ROI nodes, as also shown in Fig. 3(c), the block matrices \mathbf{C}_{bi} and \mathbf{C}_{ii} are zero matrices. Accordingly, it follows from (7) that

$$\mathbf{f}_b = (\mathbf{K}_{bb} + \mathbf{C}_{bb})\mathbf{u}_b + \mathbf{K}_{bi}\mathbf{u}_i. \quad (8)$$

Note that the nodal forces are zero on all boundary nodes except for the interacted ROI nodes. Then, by using *prime* to indicate matrices where the rows corresponding to manipulated ROI boundary nodes are removed, (8) can be rewritten as

$$(\mathbf{K}'_{bb} + \mathbf{C}'_{bb})\mathbf{u}_b + \mathbf{K}'_{bi}\mathbf{u}_i = \mathbf{0} \quad (9)$$

$$\mathbf{C}'_{bb}\mathbf{u}_b = -(\mathbf{K}'_{bb}\mathbf{u}_b + \mathbf{K}'_{bi}\mathbf{u}_i). \quad (10)$$

For known region geometry and elasticity parametrization within the ROI, the stiffness matrices \mathbf{K}'_{bb} and \mathbf{K}'_{bi} are known. Then, if we can observe a deformed state, therewith the displacement vectors \mathbf{u}_b and \mathbf{u}_i , we can then compute the right-hand-side of (10), hereafter represented with the column vector $\mathbf{b} = -(\mathbf{K}'_{bb}\mathbf{u}_b + \mathbf{K}'_{bi}\mathbf{u}_i)$. The left-hand-side of (10) can then be rewritten for knowns \mathbf{u}_b and unknowns \mathbf{C}'_{bb} , and given sufficient number of observations this system of equations can be solved.

2.4. Approximations to Compliance Boundary Conditions

Assuming a ROI model with n boundary nodes, $\mathbf{C}_{bb} \in \mathbb{R}^{Dn \times Dn}$, and despite its sparsity in practice, \mathbf{C}_{bb} may then have up to $(Dn)^2$ unknowns. Since the displacement observations cannot be arbitrarily many and Dn linearly-independent observations are

not practical, a robust reconstruction of the full \mathbf{C}_{bb} matrix is thus not realistic in practice. Nevertheless, one can observe in Fig. 3(c) that many nonzero elements lie on the block diagonal of \mathbf{C}_{bb} . For instance, the block diagonal of \mathbf{C}_{bb} has 51% of the ℓ_1 -norm of entire \mathbf{C}_{bb} . Accordingly, we propose to approximate this matrix purely as a block-diagonal matrix, calling this approximation “*block*”. As such, each boundary node in (10) is then assumed to be linearly independent from one another, leading to a CBC reconstruction of boundary node j in 3D as

$$\underbrace{\begin{bmatrix} c_{j,1} & c_{j,4} & c_{j,5} \\ c_{j,4} & c_{j,2} & c_{j,6} \\ c_{j,5} & c_{j,6} & c_{j,3} \end{bmatrix}}_{\mathbf{C}_j} \begin{bmatrix} u_{j,x} \\ u_{j,y} \\ u_{j,z} \end{bmatrix} = \begin{bmatrix} b_{j,x} \\ b_{j,y} \\ b_{j,z} \end{bmatrix}, \quad (11)$$

where symmetric semi-definite \mathbf{C}_j contains 6 unique elements encoding the compliance constraints for boundary node j . The displacement vector $[u_{j,x}, u_{j,y}, u_{j,z}]^T$ contains displacements of boundary node j in x-, y-, and z- directions, respectively. Estimating the compliance constraints in (11) can be written as linear problem

$$\underbrace{\begin{bmatrix} u_{j,x} & 0 & 0 & u_{j,y} & u_{j,z} & 0 \\ 0 & u_{j,y} & 0 & u_{j,x} & 0 & u_{j,z} \\ 0 & 0 & u_{j,z} & 0 & u_{j,x} & u_{j,y} \end{bmatrix}}_{\mathbf{A}_{j,m}} \underbrace{\begin{bmatrix} c_{j,1} \\ c_{j,2} \\ c_{j,3} \\ c_{j,4} \\ c_{j,5} \\ c_{j,6} \end{bmatrix}}_{\mathbf{c}_j} = \underbrace{\begin{bmatrix} b_{j,x} \\ b_{j,y} \\ b_{j,z} \end{bmatrix}}_{\mathbf{b}_{j,m}}. \quad (12)$$

where m represents a particular deformation observation. Then, from a total of M displacement observations with $m \in \{1, \dots, M\}$, the elements of \mathbf{c}_j can be approximated robustly in a least-squares sense using pseudo-inverse, i.e.

$$\mathbf{c}_j = (\mathbf{A}_j^T \mathbf{A}_j)^{-1} \mathbf{A}_j^T \mathbf{b}_j \quad (13)$$

where $\mathbf{A}_j = [\mathbf{A}_{j,1}^T \dots \mathbf{A}_{j,M}^T]^T$ and $\mathbf{b}_j = [\mathbf{b}_{j,1}^T \dots \mathbf{b}_{j,M}^T]^T$. At least D linearly independent deformation observations are needed to uniquely solve for *block* unknowns. For example, observations of two compressions at the same surface point and in the same direction but with different magnitudes will not be linearly independent.

We observed that the largest elements of \mathbf{C}_{bb} actually lie along the diagonal itself. For instance, ℓ_1 -norm of diagonal in Fig. 3(c) is 48% of that of entire matrix. Thus, we further propose to approximate \mathbf{C}_{bb} as only a diagonal matrix (*diag*), as a simpler and more robust alternative to *block* approximation above. This equates to $c_{j,4}=c_{j,5}=c_{j,6}=0$, where the other three constraints can be approximated by simple division, even from a single observation alone. For more observations, the above pseudo-inverse formulation can still be used, although such least-squares approximation is equivalent to the mean of individual observation estimates.

As an intuition for the above, note that the three diagonal elements of \mathbf{C}_j in the *diag* model represent axis-aligned springs (compliance elements) attached to node j ,

emulating/approximating the (lumped) effect of outer tissue and boundary conditions on that node, as illustrated in Fig. 3(d). In fact, the division for their approximation is to find such spring constants from given force (b) and displacements (u) pairs. On the other hand, the *block* model represents an arbitrary compliance formulation (not necessarily axis-aligned). Considering an eigen-decomposition of real symmetric \mathbf{C}_j , three orthogonal eigenvectors yield three directions in which three springs are attached to boundary node j , each having a spring constant of the corresponding eigenvalue. The latter naturally is more flexible as a lumped compliance approximation to outside tissue, while also requiring more measurements to characterize. Indeed, going from diagonal elements *diag* to block-diagonal *block* requires an increase in the number of variables (e.g., $2n$ -to- $3n$ in 2D and $3n$ -to- $6n$ in 3D, considering matrix symmetry), while only negligibly increasing the additional information represented by the matrix \mathbf{C}_{bb} . For instance, in the example in Fig. 3(c) *block* increases the number of variables by 50% compared to *diag*, while only representing $51-48=3\%$ more of the boundary effects.

2.5. Estimating CBC for Nonlinear Materials

The above formulations employ linear stress-strain assumption. Although the tissue is known not to be linearly elastic over large strain ranges, the linear approximation is still commonly used successfully for small displacements, such as in elastography (Wilson and Robinson 1982; Eskandari et al. 2008). Nevertheless, for large displacement scenarios, linearized approximation to nonlinear behaviour might not be accurate (Bathe et al. 1975; Zhuang and Cann 1999; DiMaio and Salcudean 2005). We hereby propose an extension of CBC for nonlinear material formulations. For such extension, we linearize the nonlinear stress-strain relation around each operating point in order to estimate CBC.

We demonstrate this CBC extension herein for a quadratic-strain stiffness matrix approximation (DiMaio and Salcudean 2005). We can express the stiffness matrix *linearized* around a deformation state \mathbf{u} , as $\mathbf{K}(\mathbf{u})$, where the linearized stiffness matrix $\mathbf{K}(\mathbf{u})$ is a function of the deformed state \mathbf{u} . For a given displacement measurement \mathbf{u} , the condensed system in (6) can then be rewritten for nonlinear materials as $\tilde{\mathbf{K}}_{oo} = \mathbf{K}(\mathbf{u}) + \mathbf{C}$, where CBC can be added on such linearized matrix, as it was shown for the linear stress-strain case above.

For a nonlinear material, \mathbf{C} can be approximated from displacement measurements as follows. For each displacement measurement \mathbf{u}_m with $m \in \{1, \dots, M\}$, we first compute the linearized stiffness matrix $\mathbf{K}(\mathbf{u}_m)$. Following the steps (7)-(9) in Section 2.3 and using $\mathbf{K}(\mathbf{u}_m)$, CBC can be approximated similarly from

$$\mathbf{C}'_{bb} \mathbf{u}_{b,m} = - (\mathbf{K}'_{bb}(\mathbf{u}_m) \mathbf{u}_{b,m} + \mathbf{K}'_{bi}(\mathbf{u}_m) \mathbf{u}_{i,m}), \quad (14)$$

where *prime* indicates the matrices where the rows corresponding to manipulated ROI boundary nodes are removed. As in (7) for linear stress-strain case, $\mathbf{K}_{bb}(\mathbf{u}_m)$, $\mathbf{K}_{bi}(\mathbf{u}_m)$, $\mathbf{u}_{b,m}$ and $\mathbf{u}_{i,m}$ are obtained with ordering the boundary ROI nodes first,

followed by the internal ROI nodes of $\mathbf{K}(\mathbf{u}_m)$ and \mathbf{u}_m , respectively. Similarly to Section 2.3, the right-hand-side of (14) is known and represented with the column vector $\mathbf{b}_m = -(\mathbf{K}'_{bb}(\mathbf{u}_m)\mathbf{u}_{b,m} + \mathbf{K}'_{bi}(\mathbf{u}_m)\mathbf{u}_{i,m})$. The left-hand-side can be reformulated as a linear problem for known \mathbf{u}_m and unknowns \mathbf{C}'_{bb} , and given sufficient number of displacement observations, this system of equations can again be solved using pseudo-inverse. Following (11) and using \mathbf{u}_m in (12), we obtain $\mathbf{A}_{j,m}$ for each boundary node j and displacement measurement m . We then approximate the elements of \mathbf{C}_j of a nonlinear material using $\mathbf{A}_j = [\mathbf{A}_{j,1}^T \cdots \mathbf{A}_{j,M}^T]^T$ and $\mathbf{b}_j = [\mathbf{b}_{j,1}^T \cdots \mathbf{b}_{j,M}^T]^T$ in (13).

3. Experiments and Results

3.1. Analytical Example

As a typical case with an analytical solution, we simulated in 2D a simple phantom of size 1×2 m with a depth of 1 m, where the model is assumed to have zero-displacement constraint in x-direction for left surface and in y-direction for bottom surface as in Fig. 4(a). Poisson’s ratio was set to 0.4999 and the Young’s modulus to 1 Pa. With the compression of the upper surface, this model is expected to deform as seen in Fig. 4(a), where the sideway elongation can be inferred analytically from Poisson’s ratio and the reaction force relates to Young’s modulus. Consider that only the top half is observed as the ROI as in Fig. 4(b), then the effect of the bottom half can be thought of springs acting on the interface nodes, i.e., finite-valued k_{1y} and k_{3y} . Assuming that the sliding boundary on the left is not observed/seen either, this should appear on the approximation as “infinite-stiffness” springs, i.e., on k_{1x} and k_{2x} . Indeed, we created such a numerical phantom, meshed with QUAD4 elements with 6 nodes and 2 elements, as in Fig. 4(c). For top compression of 5 cm, CBC was then estimated using *diag* as given in Fig. 4(d). As seen, CBC-approximated stiffness values are as expected above, practically modeling the “cushioning” effect from the unobserved tissue below.

3.2. Experimental Setup and Evaluation

For evaluating the proposed *block* and *diag* models for CBC, we conducted a simulation study with 2D and 3D numerical phantoms, as well as experiments with tissue-mimicking gelatin phantoms using deformation estimated from ultrasound images. In order to study the effect of boundary conditions, and in particular CBC, on the planning and execution of a typical computer-assisted procedure, we also simulated prostate brachytherapy needle interaction on a male pelvic anatomical model and evaluated needle targeting errors with and without CBC.

For numerical simulations, we considered a large (complete) model \mathcal{M}_f of anatomy/object and applied prescribed interactions on it in order to simulate a set of deformation observations required for CBC estimation within a smaller ROI. The interactions were chosen to be physically feasible and non-redundant (linearly independent). ROI was selected to mimic the imaging modality envisioned to acquire

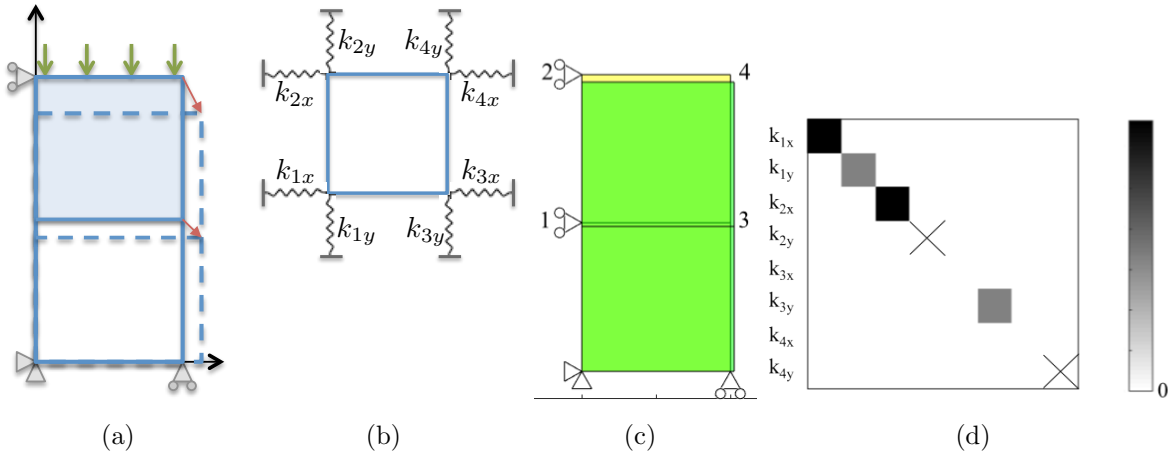


Figure 4. (a) An analytical example. If only the top half is observed as the ROI, the effect of its surrounding can be approximated as springs shown in (b). Based on a numerical simulation in (c), we estimated *diag* CBC as in (d), demonstrating k_{1x} and k_{2x} being very large successfully approximating the zero-displacement constraints whereas k_{2y} and k_{3y} having a finite stiffness approximating the “cushioning” effect of the missing part. Crosses indicate the perturbed DOF where an approximation cannot be derived (assuming reaction forces being unavailable).

observations, i.e. ROI near the object surface considering ultrasound acquisition herein. In brachytherapy the prostate is observed using transrectal ultrasound, so the ROI was set surrounding the prostate. Using these deformation observations, we then estimated CBC for a reduced model within the ROI, in order to generate an augmented reduced model \mathcal{M}_r .

For evaluations, we compared deformations predicted by \mathcal{M}_r to ground-truth deformations from \mathcal{M}_f . We used a set of interactions realistic to apply and expect in clinical scenarios (e.g. palpation on skin and insertion of a needle). For each interaction we computed ground-truth nodal displacements \mathbf{d} using \mathcal{M}_f and predicted nodal displacements \mathbf{u} using the CBC-augmented \mathcal{M}_r . We report herein average error for all nodes as

$$\mathbf{e} = \frac{\sum_{j=1}^N \delta_j}{N}, \quad (15)$$

where N is the total number of FEM nodes in ROI and δ_j is the Euclidean distance between the predicted and ground-truth displacements at node j , i.e. $\delta_j = \|\mathbf{u}_j - \mathbf{d}_j\|_2$. Since error magnitudes will be a function of overall deformation magnitudes, we also report errors normalized for each particular interaction to the maximum nodal displacement (often the palpation/interaction magnitude) d_0 , i.e.

$$\mathbf{e}_{\%} = 100 \frac{\sum_{j=1}^N \delta_j}{N \cdot d_0}. \quad (16)$$

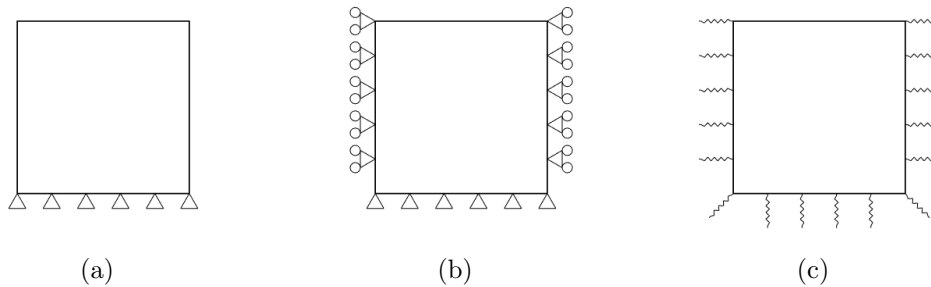


Figure 5. Boundary condition comparison: (a) *BotFix*: Fixed at the bottom surface, free on the sides. (b) *AllFix*: Fixed at the bottom surface, sliding (fixed in normal direction) for the sides. (c) *CBC*: Proposed compliance boundary conditions.

3.3. Numerical 2D Phantom

First we evaluated our method in 2D on a 140×160 mm numerical phantom with a depth of 10 mm, of which 60×80 mm on top is defined as the ROI as seen in Fig. 3(a). Poisson’s ratio and Young’s modulus were set to 0.49 to 10 kPa, respectively. The full model \mathcal{M}_f was assumed to have zero-displacement constraint at the bottom surface, and free on the sides. To compare the results with CBC, we also present baseline results with two conventional BC choices; namely (*BotFix*) where the bottom of \mathcal{M}_r is fixed, i.e. zero-displacement constraints for bottom surface in all directions, and (*AllFix*) where the two sides were also displacement constrained in the normal direction. These boundary conditions and CBC are demonstrated for 2D in Fig. 5.

For observations and evaluations, compressions of 0.3% were applied on the top surface, allowing for small-strain linear approximations for the numerical experiments. To study any effect of FEM discretization and integration choice, we used both triangular and rectangular FEM elements, both with linear and quadratic basis functions. Number of FEM nodes for each model are listed in Table 1, where TRI3 and TRI6 represent 3- and 6-node triangular, and QUAD4 and QUAD9 represent 4- and 9-node quadrilateral elements, respectively.

We first tested an ideal scenario, where we used the same surface nodes for both observations and the evaluation (called *sOE* in results). Arrows indicate the manipulated nodes. Note that, for a linear deformation model, the response for interactions on the same nodes scales linearly, so estimated displacement would simply be a linear combination of deformation observations; equivalently but without

Table 1. Number of nodes in full (\mathcal{M}_f) and reduced (\mathcal{M}_r) FEM model for palpation experiments in 2D.

Model	TRI3	TRI6	QUAD4	QUAD9
\mathcal{M}_f	479	1853	255	957
\mathcal{M}_r	111	413	63	221

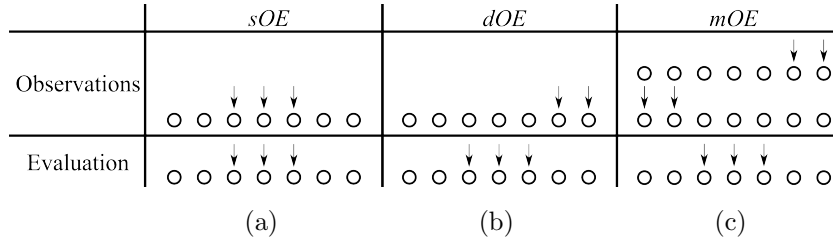


Figure 6. Different interaction scenarios for experiments are shown. (a) Same nodes (*sOE*) and (b) different nodes (*dOE*) are manipulated for observations and evaluation. (c) Multiple locations (*mOE*) are manipulated for observations, also different than evaluation.

explicitly estimating CBC. We next evaluated a more realistic scenario where the interaction location is **d**ifferent for **o**bservations and the **e**valuation (*dOE*). Note that, since each observation is a linear combination of $M-1$ others, increasing M does not yield more linearly-independent observations. Finally, to study the effect of increased linearly-independent observations, we acquired observations from interactions at **m**ultiple locations (*mOE*). The experimental scenarios above are demonstrated in Fig. 6 considering a mesh setup with 7 ROI surface nodes.

To simulate interactions for observations or evaluations, we applied several compressions $s_j = [s_{j,x}, s_{j,y}]^T$ at selected surface nodes. To apply S compressions systematically in different directions, we chose $s_j = d_0 [\cos(\pi j/S), \sin(\pi j/S)]^T$, where d_0 is the interaction magnitude and $j=\{1, \dots, S\}$.

To simulate noise in displacement observations in real applications, e.g. due to imaging and motion estimation errors, we additionally studied each scenario by adding a 20 dB uniform noise on displacement observations used for CBC reconstruction.

Table 2 shows normalized average error for CBC and conventional BC settings for different FEM element formulations. We computed $S = 10$ different compressions, and used $M = 3$ of those ten as observations (measurements) while using the remaining 7 compression experiments for evaluation by reporting their average error. The results for *sOE* experiment are given here as a form of lower-bound for error, since the observations and evaluations are from interactions at exact same points, which should anyhow correlate linearly. The *sOE* errors then represent best case fitting errors for a given model and experimental setup. Errors in all tests were lower with *mOE* compared to *dOE*, as expected, due to the higher number of observations with the latter. Comparing CBC estimation alternatives, *diag* in general yields satisfactory results, with lower errors than *block* for *sOE* and *dOE* setups, whereas the more expressive *block* model performs better with increasing number of linearly-independent observations in the *mOE* experiment. Note that *block* model has higher degrees-of-freedom, which requires a higher number of independent observations to estimate boundary conditions robustly. Errors for different FEM element types were observed to be similar, indicating that the proposed method generalizes well to different FEM element types. For evaluating the effect of noise, mean and standard deviation (in brackets) of the normalized average

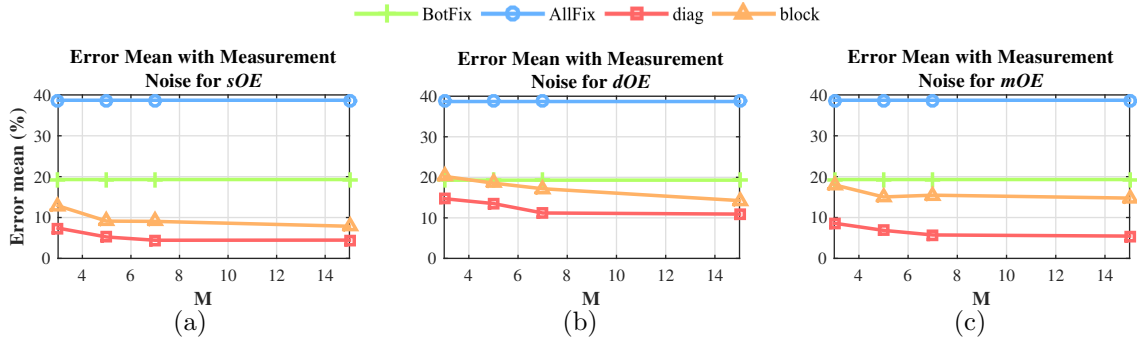


Figure 7. Normalized average error ($e\%$) for different number of observations for estimating CBC in 2D using TET3 elements for (a) sOE , (b) dOE , and (c) mOE .

error of 10 different noise realizations were reported in the table. Note that increasing the number of observations is expected to have a more substantial effect for noisy observations due to the least-squares parameter estimation: Normalized average error for changing number of M is shown in Fig. 8 for 2D.

Next, we evaluated CBC estimation for nonlinear materials. For this purpose, we used the same full model \mathcal{M}_f , reduced model \mathcal{M}_r , Poisson’s ratio, Young’s modulus, and displacement constraints for \mathcal{M}_f as in Section 3.3. CBC was compared with the same conventional choices, $BotFix$ and $AllFix$; again in three different experimental scenarios, sOE , dOE , and mOE . We simulated five deformations up to a compression of 25% strain with increments of 5%. Herein, the tissue is assumed to have a quadratic stress-strain relation in the ground-truth simulations, and we compared CBC estimation results using linear- or quadratic-strain assumptions for the ROI model \mathcal{M}_r . Fig. 8(a)-

Table 2. Average error normalized to the maximum displacement for the 2D numerical phantom with and without observation noise using different FEM element types for two conventional methods $BotFix$ and $AllFix$ and our proposed CBC.

		TRI3						TRI6					
		Error:		CBC				Error:		CBC			
		mean(std) [%]		noise-free		with noise		mean(std) [%]		noise-free		with noise	
		$BotFix$	$AllFix$	$diag$	$block$	$diag$	$block$	$BotFix$	$AllFix$	$diag$	$block$	$diag$	$block$
sOE				2.0	2.8	5.4(2.4)	10.5(5.0)			2.0	2.2	4.8(2.5)	11.4(5.4)
dOE	19.5	38.9	8.6	12.3	11.3(4.1)	20.2(8.9)	19.1	39.0	8.2	9.4	12.0(4.4)	18.4(7.4)	
mOE			5.2	4.6	6.5(2.4)	12.6(5.3)			3.6	2.8	5.5(2.5)	14.7(5.9)	

		QUAD4						QUAD9					
		Error:		CBC				Error:		CBC			
		mean(std) [%]		noise-free		with noise		mean(std) [%]		noise-free		with noise	
		$BotFix$	$AllFix$	$diag$	$block$	$diag$	$block$	$BotFix$	$AllFix$	$diag$	$block$	$diag$	$block$
sOE				2.1	2.2	4.2(1.8)	6.8(4.3)			2.0	2.2	4.1(1.7)	6.7(4.2)
dOE	19.5	38.6	8.9	10.4	9.0(3.6)	22.4(7.4)	19.1	38.8	8.3	9.8	10.4(4.2)	26.0(8.2)	
mOE			5.2	4.3	4.9(1.6)	10.8(4.1)			3.8	2.9	6.0(2.9)	16.2(6.2)	

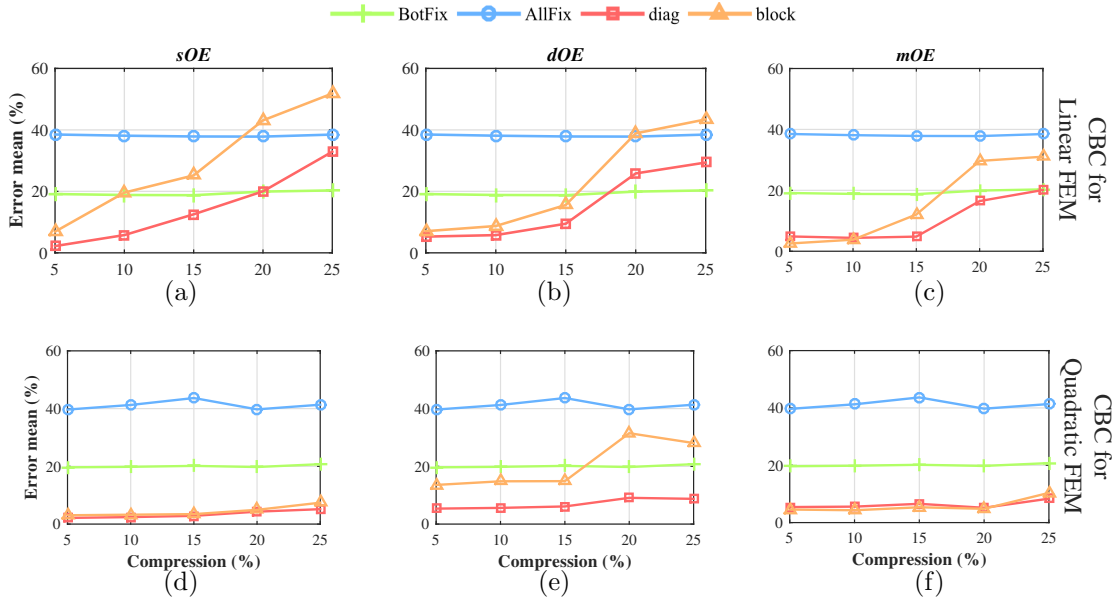


Figure 8. Normalized average error ($e\%$) for different compression magnitudes for 2D TET3 elements. The full model was simulated using quadratic stress-strain assumption. For the ROI model, (a)-(c) use (false) linear stress-strain assumption when estimating CBC, while (d)-(f) use (correct) quadratic stress-strain assumption.

8(c) show normalized average error for linear stress-strain relation. Results demonstrate that CBC errors increase at higher compression amplitudes due to the incorrect stress-strain assumption, while the conventional techniques yield a relatively constant error after normalization. Indeed, after some point ($\approx > 15\%$ strain) CBC with this false linear assumption yields poorer deformation estimation than conventional settings. Fig. 8(d)-8(f) show normalized average error for CBC with quadratic stress-strain relation, with results showing that errors stay low with CBC even at relatively high strains; *diag* being the robust option as was also repeatedly shown earlier. This demonstrates that for nonlinear materials with large compression amplitudes, our nonlinear CBC estimation technique is required and performs successfully.

3.4. Numerical 3D Phantom

Next, we evaluated a similar scenario in 3D. A $140 \times 140 \times 160$ mm numerical phantom was constructed with linear 4-node tetrahedral (TET4) and 8-node hexahedral (HEX8) elements, with a $60 \times 60 \times 80$ mm section being the ROI. The full model contains 3825 nodes, whereas the reduced model includes 441 nodes. Poisson's ratio was set to 0.49 and Young's modulus to 10 kPa. Compressions of 0.3% were applied for observation and evaluation using linear stress-strain assumption. The full model was assumed to have zero-displacement constrained at the bottom surface. Same baseline comparisons, *BotFix* and *AllFix*, for ROI were evaluated.

For displacement observations and evaluations, again S compressions each with magnitude d_0 were applied in directions $[\sin \theta_j \cos \phi_k, \sin \theta_j \sin \phi_k, \cos \theta_j]$ for elevation

angle $\theta_j=(\pi j/P)$ and azimuth angle $\phi_k=(2\pi k/Q)$ where $j=\{1, \dots, P\}$, $k=\{1, \dots, Q\}$ and $S=P \cdot Q$. Below, we repeated *sOE*, *dOE*, and *mOE* experiments in 3D, also with noise.

Normalized average error for $P=Q=3$ are shown in Table 3 for 3D using TET4 and HEX8 FEM elements. *diag* yields the least error error for for all experiments. Increasing number of linearly-independent observations decreases error for *block* more significantly than *diag*, although the latter still achieving better. Potentially, additional indentation locations could reduce this error further, even below *diag*. For evaluating the effect of noise, results from an average of 10 different noise realizations are also shown in this results table for 3D. It is seen that for increased number of linearly-independent noisy observations, *diag* yields the best results. As in 2D, the normalized average error for different types of FEM elements are similar, indicating the independence of CBC from element type.

Note that, boundary estimation in Matlab takes under 10 ms in 2D and under 50ms in 3D, which is a feasible time-frame to include in intra-operative planning simulations.

3.5. Numerical Simulation of Commercial CIRS Elasticity Phantom

We further evaluated our method with a numerical simulation of CIRS Elasticity QA Phantom Model 049 (Computerized Imaging Reference Systems, Norvolk, USA). The aim of this experiment is to evaluate CBC using the known elasticity parameters. A $180 \times 120 \times 95$ mm numerical phantom was constructed based on CIRS phantom design specifications using a mesh generation toolbox Fang and Boas 2009 as in Fig. 9(a). A $30 \times 40 \times 45$ mm part was defined as the ROI as shown in Fig. 9(b). The full model contains 24976 nodes and 137220 tetrahedral elements, and the ROI model has 875 nodes and 3639 tetrahedral elements. The numerical phantom contains two sizes of spheres (5 mm and 10 mm radius) which are located at two different depths (15 mm and 35 mm). At each depth there are four spherical inclusions with Young’s modulus of 8 kPa, 14 kPa, 45 kPa, and 80 kPa, respectively, where the background is 25 kPa, according to phantom specs. Poisson’s ratio was set to 0.49. The full model was zero-displacement constrained at the bottom surface, and for the sides in the normal direction.

Deformation was applied by indenting selected surface nodes of ROI by a fixed

Table 3. Average error normalized to maximum displacement for the 3D numerical phantom using different FEM element types for conventional methods and CBC.

	TET4						HEX8					
	Error:		CBC				Error:		CBC			
	mean(std) [%]		noise-free		with noise		mean(std) [%]		noise-free		with noise	
	<i>BotFix</i>	<i>AllFix</i>	<i>diag</i>	<i>block</i>	<i>diag</i>	<i>block</i>	<i>BotFix</i>	<i>AllFix</i>	<i>diag</i>	<i>block</i>	<i>diag</i>	<i>block</i>
<i>sOE</i>			6.7	7.2	7.4(4.8)	33.0(9.2)			6.3	7.3	8.6(5.2)	30.7(8.4)
<i>dOE</i>	13.9	29.5	7.3	9.4	23.8(5.6)	35.1(10.2)	13.4	28.0	7.3	9.2	19.8(4.6)	36.9(10.1)
<i>mOE</i>			5.9	6.5	6.4(2.7)	15.7(4.5)			5.6	6.6	7.5(3.0)	12.1(4.6)

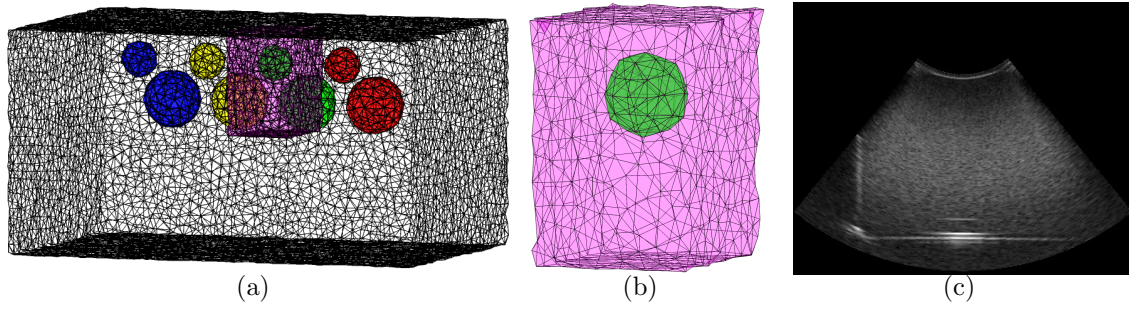


Figure 9. (a) A mesh model of CIRS Elasticity phantom is shown. Blue, yellow, green, and red spheres, respectively, have Young’s moduli of 8, 14, 45, and 80 kPa. The defined ROI box is shown in purple. (b) A close-up of ROI. (c) A B-mode US image showing the ROI.

amplitude in the normal direction, simulating ultrasound probe indentation. For CBC reconstruction observations, we simulated five deformations up to a compression of 0.25% strain with increments of 0.05%. For evaluations, deformation observations were collected by indenting ten different ROI surface nodes individually by 0.5% strain. Due to small displacements, we used CBC estimation with linear-strain stiffness matrix. Table 4 shows normalized average error. Since for many clinical applications a target anatomy is of concern, we also evaluated the nodes within the spherical inclusion, which herein models a target anatomy. Results show that *diag* yields half the average error compared to conventional boundary constraint formulations, both for the inclusion nodes as well as for the entire ROI.

3.6. Gelatin Phantom

Next we evaluated our method using image data. Since the inclusions in CIRS Elasticity QA Phantom above have by design no contrast in B-mode US images, cf. Fig. 9(c), these could not be used as internal image features for evaluation. Therefore, we used US images from a custom-made tissue-mimicking gelatin phantom of size $60 \times 90 \times 90$ mm. This had a soft cylindrical inclusion of 25 mm diameter, manufactured as hypoechogenic using reduced scattering material (cellulose). The phantom was imaged using a linear-array US transducer, where the acquired images are of size 37.5×70 mm with a resolution of 220×410 as shown in Fig. 10. Eleven images were acquired, for which the phantom was compressed with 1 mm increments up to 10 mm compression. Three sample US

Table 4. Normalized average error comparison of conventional boundary conditions and CBC for the CIRS elasticity QA phantom experiment.

Avg Error [%]	Conventional		CBC	
	<i>BotFix</i>	<i>AllFix</i>	<i>diag</i>	<i>block</i>
All ROI nodes	11.8	12.8	5.8	15.2
Only inclusion nodes	9.2	17.0	5.5	6.9

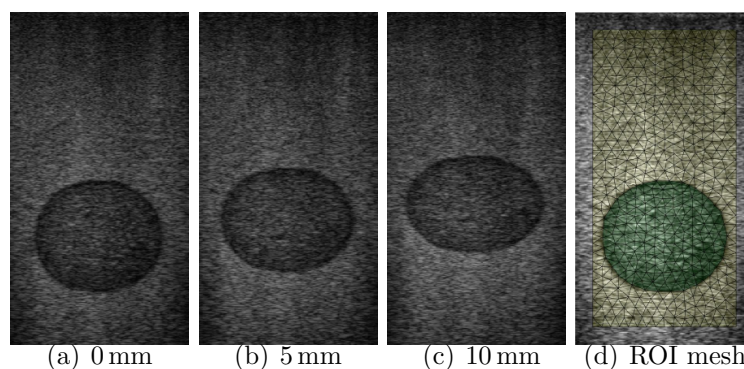


Figure 10. US images obtained from a tissue-mimicking gelatin phantom with 0, 5, and 10 mm indentations are shown, also showing the overlay of a ROI mesh.

images acquired at 0, 5, and 10 mm indentations are shown in Fig.10(a)-(c).

The ROI was modeled from the US image at 0 mm indentation and was meshed by a 2D meshing toolbox (Engwirda 2015), which yielded 495 nodes and 892 triangular elements shown in Fig. 10(d). For deformation, we used a 2D plane-strain approximation. Young’s modulus was set to 15 kPa for background and 5 kPa for the inclusion based on gelatin concentrations used. Poisson’s ratio was set to 0.48. We then measured displacement fields over the image between all pairs of 11 images using Jones et al. 2014.

Similarly to earlier experiments, we used displacements from US image pairs both for obtaining CBC observations and as ground-truth displacements for evaluations in a leave-one-out fashion: We estimated CBC using observations from nine compressions, and the excluded US image was used for evaluation with the CBC predicted from the former. Due to larger displacements in observation and evaluation phases, we repeated this experiments using linear and nonlinear strain assumptions, the latter as in Section 2.5. Table 5 shows prediction errors for all ROI nodes as well as for only the nodes within the soft inclusion. These indicate that *diag* approximation of CBC yields superior deformation prediction compared to conventional heuristic boundary settings.

Table 5. Average error comparison of conventional boundary conditions and CBC for the gelatin phantom.

Boundary Conditions		Linear stiffness matrix			
		Normalized Error [%]		Error [mm]	
		ROI	Inclusion	ROI	Inclusion
Conventional	<i>BotFix</i>	25.6	27.6	1.4	1.5
	<i>AllFix</i>	25.6	28.9	1.4	1.6
CBC	<i>diag</i>	17.2	14.8	1.0	0.8
	<i>block</i>	45.5	19.8	2.4	1.0

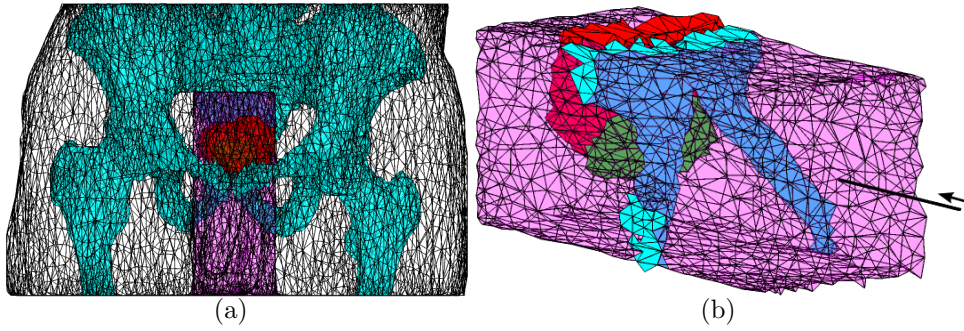


Figure 11. (a) Full model of male pelvic anatomy with prostate (green), the bones (cyan), bladder (red), and soft tissue (white). (b) Reduced ROI model (magenta) also showing needle insertion.

3.7. Male Pelvic Anatomical Model

Next, we consider a computer-assisted intervention scenario, where the interaction of a needle and a male pelvic anatomical model is simulated and analyzed using CBC. Male pelvic model was obtained by 3D meshing segmented MR images using (Fang and Boas 2009). The full model had an extent of $432 \times 290 \times 273$ mm, meshed with 17949 nodes and 93388 tetrahedral elements, including models of the prostate, bladder, and pelvic and hip bones, as well as the remaining volume filled with periprostatic soft tissue as seen in Fig. 11(a). For the reduced ROI model, we considered a region from the skin toward the prostate, within which needle interactions and relevant prostate deformation occur. This ROI lies superior to where a template is often placed during prostate interventions. ROI mesh included 1896 nodes and 8363 tetrahedral elements as in Fig. 11(b). Poisson’s ratio was set to 0.49. Young’s modulus was set to 20 kPa for the prostate, 10 kPa for the bladder, and 15 kPa for the remaining elements as in Chai et al. 2011. Nodes on the pelvic bone were set as zero-displacement constrained. Patient table was mimicked using zero-displacement constraints on anterior nodes of the model. Two baseline comparisons were performed; *OnlyBone* using zero-displacement constraints on pelvic bone nodes, and *AllFix* by additionally fixing all around ROI model similarly to other experiments.

For displacement observations to estimate CBC, we used $M = 10$ palpations on the skin (which theoretically could be performed with a tool or the finger in the operating room). We then simulated $S = 10$ needle insertions targeted at random locations within the prostate by applying some displacement on the nodes along the needle shaft in the insertion direction. This simulates the static friction between the needle and the tissue similarly to “stuck state” in (Goksel et al. 2011). We herein distributed this effect to tissue nodes near the needle shaft within a margin of R , chosen such that the displaced (contact) nodes along the shaft have a distribution of approximately the tissue mesh resolution. A given external (insertion) magnitude is then distributed to those nodes inversely-proportional to their distance to the needle shaft. Table 6 shows average errors when 2.5 mm displacement is applied. We evaluated displacement errors in the

entire ROI as well as only at the needle tip, since the needle tip location is important for many clinical applications such as biopsy and brachytherapy. Results indicate that *diag* yields lowest error values for any metric and scenario. Considering needle targeting errors, CBC results in a quarter to half of the errors compared to conventional boundary formulations.

4. Discussion and Conclusions

We have demonstrated compliance boundary conditions (CBC) to model boundary constraints that are parametrized from observed tissue displacements. Our evaluations using numerical models and real image data show that the proposed method CBC can estimate deformations more accurately than the conventional boundary condition settings. Comparing different proposed approximations, the diagonal model *diag* is seen to be the more robust approach with accurate deformation simulations.

Note that CBC is a generalization of the boundary conditions introduced in Cotin et al. 1996, where the springs attached to the boundary nodes have an empirically-set stiffness and infinite length. In our work, we propose an approach to parametrize those experimentally by exploiting observed deformations. Our proposed method is also a generalization of conventional boundary constraints, where zero-displacement and -force constraints are obtained at the two extremes of the CBC parameter, which acts as a spring constant. The two extremes, such as zero-displacement for fixed *rigid* structures and zero-force for *free* air can be captured with very large (∞) and infinitesimal (ϵ) spring stiffness.

In contrast to conventional approaches, CBC requires deformation observations and, thus, may be limited by the noise in such measurements. Nevertheless, multiple observations can be collected by medical imaging as shown in this paper; which help increase SNR of CBC approximations. Ideally, deformation observations with different interaction points are needed, which is our *mOE* experimental setting – also as a realistic and desirable clinical scenario. In most practical clinical applications such as computer-assisted interventions, the clinician already interacts with the tissue and different forms of multiple tissue interactions are fortunately common. Hence, there are natural scenarios where such displacement observations can be collected in practice. Different

Table 6. Average error comparison of conventional boundary conditions and CBC, for needle insertion experiments in a male pelvic anatomical model.

Boundary Conditions		Normalized Error [%]		Error [mm]	
		Entire ROI	Needle tip	Entire ROI	Needle tip
Conventional	<i>OnlyBone</i>	139.8	105.0	3.5	2.6
	<i>AllFix</i>	39.9	50.6	1.0	1.2
CBC	<i>diag</i>	37.1	27.5	0.9	0.7
	<i>block</i>	74.7	31.2	1.8	0.8

forms of multiple tissue interactions are fortunately common (and often a surgical necessity) in most computer-assisted interventions, hence conducting such observations is not a major limitation. Although linear-independence of observations is prescribed for a complete 3D CBC estimation, boundary effects can also still be captured for a limited range of interactions (e.g., at the same location or in the same direction) only from observations for that location/direction.

In estimating CBC, we assume that the elasticity distribution within the ROI is given. In practice, this is typically extracted by segmenting the anatomy (also possibly automatically) and using elastic properties reported in the literature for each tissue type. Alternatively, image registration (Soza et al. 2005; Lee et al. 2012) or *elastography* (Kallel and Ophir 1997; Dooley et al. 2000; Manduca et al. 2001; Goksel et al. 2013) can be used to reconstruct patient-specific elastic distributions. Additionally, we treat the anatomy as a purely compressible medium, although sliding between organs due to breathing might occur, especially in the viscera (Goksel et al. 2016).

Note that estimating CBC with nonlinear stiffness matrix does not require any additional information compared to linear stress-strain version, besides an increased number of observations to robustly capture nonlinear effects. Our results show that, for nonlinear materials with large strains, our nonlinear CBC estimation strategy yields satisfactory results. Additionally, the formulation in Section 2.5 assumes linear springs in CBC. This can, nevertheless, be easily extended to nonlinear springs, such as for quadratic CBC springs $ku^2=f$, each element of $\mathbf{A}_{j,m}$ in (12) needs to be squared for each measurement before being used in (13) for CBC approximation.

CBC has been shown to yield substantially more accurate deformation estimations, which are essential for patient-specific tissue deformation simulations for pre-operative planning and intra-operative guidance of medical interventions. To the best of our knowledge, our technique is the first for modeling boundary conditions parametrically to estimate them empirically using medical imaging data. CBC can be embedded into standard models without increasing computation time, since augmenting a stiffness matrix with CBC involves mere additions in an offline stage and it does not change the size of the stiffness matrix. Furthermore, estimating CBC is a very quick and constant time operation for each node, since CBC parametrization of each boundary node is linearly independent and can be performed in parallel. Note that the proposed CBC augmentation can be naturally extended to dynamic FEM models, where only the stiffness matrix is augmented with CBC as given. Investigating CBC in different clinical application scenarios together with in-vivo experiments will be the focus of future work.

Acknowledgments

This work was funded by the Swiss National Science Foundation (SNSF). The authors thank Maxim Makhinya for his support in data collection.

References

- Ahmadian, H., Mottershead, J., and Friswell, M. (2001). “Boundary Condition Identification By Solving Characteristic Equations”. In: *Journal of Sound and Vibration* 247(5), pp. 755–763.
- Ayache, N., Cotin, S., Delingette, H., Clement, J.-M., Marescaux, J., and Nord, M. (1998). “Simulation of Endoscopic Surgery”. In: *Journal of the Society for Minimally Invasive Therapy and Allied Technologies* 7(2), pp. 71–77.
- Bathe, K. J., Ramm, E., and Wilson, E. L. (1975). “Finite Element Formulations for Large Deformation Dynamic Analysis”. In: *Int. Journal for Numerical Methods in Engineering* 9, pp. 353–386.
- Becker, M. and Teschner, M. (2007). “Robust and Efficient Estimation of Elasticity Parameters using the Linear Finite Element Method”. In: *Procs. Conference on Simulation and Visualization*.
- Bro-Nielsen, M. and Cotin, S. (1996). “Real-time Volumetric Deformable Models for Surgery Simulation using Finite Elements and Condensation”. In: *Procs. Eurographics*, pp. 57–66.
- Chai, X., Herk, M. van, Kamer, J. van de, Hulshof M.C. and Remeijer, P., Lotz, H., and Bel, A. (2011). “Finite element based bladder modeling for image-guided radiotherapy of bladder cancer”. In: *Journal of Medical Physics* 38, pp. 142–150.
- Clifford, M. A., Banovac, F., Levy, E., and Cleary, K. (2002). “Assessment of Hepatic Motion Secondary to Respiration for Computer Assisted Interventions”. In: *Computer Aided Surgery* 7, pp. 291–299.
- Cotin, S., Delingette, H., and Ayache, N. (1996). “Real time volumetric deformable models for surgery simulation”. In: *Visualization in Biomedical Computing*. Springer Berlin Heidelberg.
- Cui, F., Liu, J., Liu, Z., Chi, Y., Liu, J., Wu, J., Qi, T., and Ho, H. S. S. (2014). “Prediction of Prostate Motion and Deformation Using FE Modeling for Better Biopsy Accuracy”. In: *Procs. European Conference on Computational Mechanics*.
- Debunne, G., Desbrun, M., Cani, M.-P., and Barr, A. H. (2001). “Dynamic Real-Time Deformations using Space & Time Adaptive Sampling”. In: *Procs. SIGGRAPH*, pp. 31–36.
- Dehghan, E., Wen, X., Zahiri-Azar, R., Marchal, M., and Salcudean, S. (2008). “Needle-tissue interaction modeling using ultrasound-based motion estimation: Phantom study.” In: *Computer Aided Surgery* 13(5), 265–280.
- Didier, A.-L., Villard, P.-F., Saade, J., Moreau, J.-M., Beuve, M., and Shariat, B. (2007). “A chest wall model based on rib kinematics”. In: *Procs. Int. Conf. on Biomedical Visualization*, pp. 159–164.
- DiMaio, S. and Salcudean, S. (2005). “Needle Steering and Motion Planning in Soft Tissues”. In: *IEEE Transactions on Biomedical Engineering* 52.6, pp. 965–974.
- Doyley, M., Meaney, P., and Bamber, J. (2000). “Evaluation of an iterative reconstruction method for quantitative elastography”. In: *Phys Med Biol* 45(6), pp. 1521–1540.
- Engquist, B. and Majda, A. (1977). “Absorbing Boundary Conditions for the Numerical Simulation of Waves”. In: *Mathematics of Computation* 31.139, pp. 629–651.
- (1979). “Radiation boundary conditions for acoustic and elastic wave calculations”. In: *Communications on Pure and Applied Mathematics* 32, pp. 313–357.
- Engwirda, D. (2015). *MESH2D*. <http://www.mathworks.com/matlabcentral/fileexchange/25555-mesh2d-automatic-mesh-generation>.
- Eom, J., Xu, X. G., and De, S. (2010). “Predictive modeling of lung motion over the entire respiratory cycle using measured pressure-volume data, 4DCT images, and finite-element analysis”. In: *Journal of Medical Physics* 37(8), pp. 4389–4400.
- Eskandari, H., Salcudean, S., Rohling, R., and Ohayon, J. (2008). “Viscoelastic characterization of soft tissue from dynamic finite element models”. In: *Phys Med Biol* 53, pp. 6569–6590.
- Fang, Q. and Boas, D. (2009). “Tetrahedral mesh generation from volumetric binary and gray-scale images”. In: *Procs. IEEE Int. Symposium on Biomedical Imaging (ISBI)*, pp. 1142–1145.
- Goksel, O. and Salcudean, S. E. (2011). “Image-based variational meshing”. In: *IEEE Transactions on Medical Imaging* 30(1), pp. 11–21.
- Goksel, O., Sapchuk, K., and Salcudean, S. E. (2011). “Haptic Simulator for Prostate Brachytherapy with Simulated Needle and Probe Interaction”. In: *IEEE Transactions on Haptics* 4, pp. 188–198.

- Goksel, O., Eskandari, H., and Salcudean, S. E. (2013). “Mesh Adaptation for Improving Elasticity Reconstruction Using the FEM Inverse Problem”. In: *IEEE Transactions on Medical Imaging* 32.2, pp. 408–418.
- Goksel, O., Vishnevsky, V., Gomariz Carrillo, A., and Tanner, C. (2016). “Imaging of Sliding Visceral Interfaces During Breathing”. In: *Procs. IEEE Int. Symposium on Biomedical Imaging (ISBI)*.
- Harders, M., Hutter, R., Rutz, A., Niederer, P., and Szekely, G. (2003). “Comparing a Simplified FEM Approach with the Mass-Spring Model for Surgery Simulation”. In: *Studies in Health Technology and Informatics* 94, pp. 103–109.
- Hensel, J., Menard, C., Chung, P., M.F., M., Kirilova, A., Moseley, J., Haider, M., and Brock, K. (2007). “Development of Multiorgan Finite Element-Based Prostate Deformation Model Enabling Registration of Endorectal Coil Magnetic Resonance Imaging for Radiotherapy Planning”. In: *International Journal of Radiation Oncology Biology Physics* 68(5), pp. 1522–1528.
- Jones, E. M. C., Silberstein, M. N., White, S. R., and Sottos, N. R. (2014). “In Situ Measurements of Strains in Composite Battery Electrodes during Electrochemical Cycling”. In: *Experimental Mechanics* 54(6), pp. 971–985.
- Kallel, F. and Ophir, J. (1997). “A least-squares strain estimator for elastography”. In: *Ultrasonic Imaging* 19(3), pp. 195–208.
- Koch, R. M., Gross, M., Carls, F., Buren, D. F. von, Fankhauser, G., and Parish, Y. (1996). “Simulating Facial Surgery Using Finite Element Models”. In: *Procs. SIGGRAPH*, pp. 421–428.
- Lasso, A., Avni, S., and Fichtinger, G. (2010). “Targeting Error Simulator for Image-guided Prostate Needle Placement”. In: *Procs. International Conference of the IEEE Engineering in Medicine and Biology Society (EMBC)*, pp. 5424–5427.
- Lee, H.-P., Foskey, M., Niethammer, M., Krajcevski, P., and Lin, M. C. (2012). “Simulation-Based Joint Estimation of Body Deformation and Elasticity Parameters for Medical Image Analysis”. In: *IEEE Transactions on Medical Imaging* 31(11), pp. 2156–2168.
- Li, M., Castillo, E., Zheng, X.-L., Luo, H.-Y., Castillo, R., Wu, Y., and Guerrero, T. (2013). “Modeling lung deformation: A combined deformable image registration method with spatially varying Young’s modulus estimates”. In: *Medical Physics and Practice* 40(8), p. 081902.
- Manduca, A., Oliphant, T., Dresner, M., Mahowald, J., Kruse, S., Amromin, E., Felmlee, J., Greenleaf, J., and Ehman, R. (2001). “Magnetic resonance elastography: Non-invasive mapping of tissue elasticity”. In: *Medical Image Analysis* 5, pp. 237–254.
- Misra, S., Macura, K., Ramesh, K., and Okamura, A. (2009). “The Importance of Organ Geometry and Boundary Constraints for Planning of Medical Interventions”. In: *Medical Engineering and Physics* 31, pp. 195–206.
- Misra, S., Ramesh, K. T., and Okamura, A. M. (2008). *Modeling of Tool-Tissue Interactions for Computer-Based Surgical Simulation: A Literature Review*. Presence (Cambridge, Mass.)
- Mollema, W., Schutyser, F., Van Cleynenbreugel, J., and Suetens, P. (2004). “Fast Soft Tissue Deformation with Tetrahedral Mass Spring Model for Maxillofacial Surgery Planning Systems”. In: *Procs. Med Image Comput Comput Assist Interv (MICCAI)*, pp. 371–379.
- Nataf, F. (2013). “Absorbing boundary conditions and perfectly matched layers in wave propagation problems”. In: *Radon Series on Computational and Applied Mathematics* 11, pp. 219–231.
- Ozkan, E. and Goksel, O. (2015). “Compliance Boundary Conditions for Simulating Deformations in a Limited Target Region”. In: *Procs. International Conference of the IEEE Engineering in Medicine and Biology Society (EMBC)*, pp. 929–932.
- Peterlik, I., Duriez, C., and Cotin, S. (2012). “Modeling and Real-Time Simulation of a Vascularized Liver Tissue”. In: *Procs. Med Image Comput Comput Assist Interv (MICCAI)*, pp. 50–57.
- Plantefeve, R., Peterlik, I., Courtecuisse, H., Trivisonne, R., Radoux, J., and Cotin, S. (2014). “Atlas-based Transfer of Boundary Conditions for Biomechanical Simulation”. In: *Procs. Med Image Comput Comput Assist Interv (MICCAI)*, pp. 33–40.

- Preiswerk, F., De Luca, V., Arnold, P., Celicanin, Z., Petrusca, L., Tanner, C., Bieri, O., Salomir, R., and Cattin, P. C. (2014). “Model-guided respiratory organ motion prediction of the liver from 2D ultrasound”. In: *Medical Image Analysis* 18(5), pp. 740–751.
- Roose, L., Loeckx, D., Mollemans, W., Maest, F., and Suetens, P. (2008). “Adaptive boundary conditions for physically based follow-up breast MR image registration”. In: *Procs. Med Image Comput Comput Assist Interv (MICCAI)*, pp. 839–846.
- Sauter, S. and Schanz, M. (2017). “Convolution quadrature for the wave equation with impedance boundary conditions”. In: *Journal of Computational Physics* 334, pp. 442–459.
- Sharma, N. and Aggarwal, L. M. (2010). “Automated medical image segmentation techniques”. In: *Journal of Medical Physics* 35.1, pp. 3–14.
- Soza, G., Grosso, R., Nimsy, C., Hastreiter, P., Fahlbusch, R., and Greiner, G. (2005). “Determination of the elasticity parameters of brain tissue with combined simulation and registration”. In: *The International Journal of Medical Robotics and Computer Assisted Surgery* 1(3), pp. 87–95.
- Wilson, L. and Robinson, D. (1982). “Ultrasonic Measurement of Small Displacements and Deformations of Tissue”. In: *Ultrasonic Imaging* 4.1, pp. 71–82.
- Zhuang, Y. and Cann, J. (1999). “Real-time Simulation of Physically Realistic Global Deformation”. In: *Procs. SIGGRAPH*.